J. Iron Steel Res. Int. (2021) 28:66–75
https://doi.org/10.1007/s42243-020-00457-2

ORIGINAL PAPER

Microstructure evolution of ultra-high-strength twinning-induced plasticity (TWIP) steel under dynamic loading

Qi-hang Pang[1,2] · Mei Xu[3] · Zhen-li Mi[4] · Juan Cui[5] · Jing Guo[1,2]

Received: 1 November 2019 / Revised: 27 March 2020 / Accepted: 29 March 2020 / Published online: 22 July 2020

Abstract
To prepare ultra-high-yield strength twinning-induced plasticity (TWIP) steel and reveal its work hardening mechanism at different strain rates from the microcosmic range, the microstructure evolution mechanism of Fe–20Mn–0.6C TWIP steel was investigated at strain rates of 10^{-4}–10^{3} s^{-1} using a high-speed tensile testing machine and a transmission electron microscope. The results show that the strain rate and deformation had a significant effect on the twin morphology of TWIP steels. At a strain rate of 10^{2} s^{-1}, secondary deformation twins were developed, which intersected with the initial deformation twins and increased the resistance of dislocation movement, as well as the plasticity. TWIP steel at a strain rate of 10^{2} s^{-1} had a higher twin formation speed than that at 10^{0} s^{-1}. At the same amount of deformation, the twin boundary fraction was higher and increased linearly at a strain rate of 10^{2} s^{-1}, while the rule of twin growth at 10^{0} s^{-1} was conformed to S-curve change of DoseResp model.

Keywords Twinning-induced plasticity steel · Electron backscattered diffraction · Microstructure · Dynamic loading · Strain rate · Work hardening

1 Introduction

In recent years, the iron and steel enterprises, such as ArcelorMittal, Thyssen in Germany, POSCO in Korea, Baosteel and Ansteel in China, have started to trial produce twinning-induced plasticity (TWIP) steel. Due to the low fault energy characteristics, excellent plasticity, and high strain hardening ability during deformation, TWIP steel shows a good application prospect [1–3]. As shown in previous experiments [4, 5], the main deformation mechanism of experimental medium manganese high-carbon steels is TWIP effect. Shen et al. [6, 7] elucidated the determining role of grain size and strain rate on the mechanical behavior of a series of twinning-induced plasticity steels (Fe–20Mn–0.6C, wt.%) with average grain size in the range of 3.5–25 μm. The steel with average grain size of 3.5 μm was characterized by true ultimate tensile strength of 1930 MPa and excellent elongation-to-failure of 66% at a strain rate of 0.005 s^{-1}. Chen et al. [8] investigated the effect of deformation temperature on the evolution of deformation twins and the mechanical properties of medium manganese high-carbon steel. It was found that the main reason for twin boundary bending was twin nucleus formation. There were the reaction of dislocation and stacking faults and the conversion of coherent and incoherent lattices at low deformation temperature.

However, there are still some technical bottlenecks in the industrial mass production and practical application of TWIP steel. One is that the yield strength of TWIP steel is low (generally 200–400 MPa) and its torsional deformation resistance is insufficient, which makes it difficult to be manufactured integrally; the other is that the deformation mechanism at high strain rate is still not clear. Some research groups [9–14] have conducted in-depth studies on

✉ Juan Cui
280100886@qq.com

1 School of Materials and Metallurgy, University of Science and Technology Liaoning, Anshan 114051, Liaoning, China

2 State Key Laboratory of Metal Material for Marine Equipment and Application, Anshan 114009, Liaoning, China

3 State Key Laboratory of Advanced Stainless Steel Materials, Taiyuan Iron and Steel Group Co., Ltd., Taiyuan 030003, Shanxi, China

4 Institute of Engineering Technology, University of Science and Technology Beijing, Beijing 100083, China

5 Beijing Jianlong Heavy Industry Group Co., Ltd., Beijing 100070, China

the mechanical behavior of TWIP steel at different strain rates, where it was revealed that TWIP steel exhibits different deformation characteristics under static, quasi-static (e.g., strain rate between 10^{-6} and 10^{-1} s^{-1}), and dynamic (e.g., strain rate between 10^{0} and 10^{3} s^{-1}) loadings. Kim et al. [15] demonstrated that dynamic strain aging was caused by the interaction between dislocation movement, solute atom, and C–Mn atom during plastic deformation. Bouaziz et al. [16] has confirmed that this phenomenon is also related to the strain rate, temperature, and other conditions associated with plastic deformation. Grässel et al. [17] and Frommeyer et al. [18] studied Fe–Mn–Si–Al alloy, which is a typical TWIP steel, and found that when Mn content is less than 20 wt.%, no strain rate sensitivity is observed. However, when Mn content exceeded 25 wt.%, TWIP steel exhibited a pronounced shift in mechanical behavior, where the flow stress increased with the increasing strain rate. Xu et al. [19] investigated the dynamic tensile behavior of Fe–23.7Mn–2.3Si–2.7Al–0.01C (wt.%) TWIP steel at low and medium strain rates (10^{-3}–4×10^{2} s^{-1}). Their results demonstrated a significant decrease in tensile strength at low strain rates (10^{-3}–10^{-2} s^{-1}). However, in the range of 10^{-2}–4×10^{2} s^{-1}, the tensile strength and hardening rate increased with the increasing strain rate.

Consequently, in this study, Fe–20Mn–0.6C TWIP steel with yield strength up to 629 MPa was prepared and its work hardening behavior at different strain rates was studied. Due to the precipitates in TWIP steel and the effect of strain rate, it will show different work hardening mechanisms at different strain rates. The microstructure evolution of ultra-high-yield strength TWIP steel at different strain rates was analyzed, and the relationship between the microstructure evolution and work hardening mechanism was revealed.

2 Materials and methods

An Fe–20.12Mn–0.59C–1.53Al–0.04Nb–0.47V–0.03Ti (wt.%) TWIP steel was prepared in a vacuum induction furnace and was cast into ingots. The ingots were sectioned into rectangular pieces (80 mm × 80 mm × 70 mm) for forging. The as-forged samples were heated at 1180 °C for 1.5 h before rolling. The initial rolling temperature was 1100 °C. After seven hot rolling passes (4 mm), the rolling temperature was reduced to 620–650 °C and the rolling process was continued until a thickness of 1.6 mm was attained. Then, the plates were heated at a heating rate of 10 °C/s to 750 °C and held for 7 min. Finally, they were cooled down to room temperature at a cooling rate of 10 °C/s.

The tensile test samples were prepared according to Chinese standards (GB/T 228.1-201 and GB/T 30069.1-2013). Then, an SANS-CMT5105 microcomputer-controlled electronic universal testing machine and a Zwick/Roell HTM16020 high-speed tensile testing machine were used to investigate the tensile behavior of TWIP steel at different strain rates, which ranged from 10^{-4} to 10^{3} s^{-1}. The samples were etched in 4 vol.% Nital solution, and their microstructure was characterized using an LEO-1450 scanning electron microscope equipped with electron backscattered diffraction (EBSD). EBSD samples were prepared using electrolytic polishing in a solution of 15% perchloric acid and 85% ethanol (vol.%). A transmission electron microscope (TEM, JEOL JEM 2000 FX) was used to characterize the morphology of the microstructure.

3 Experimental results

3.1 Mechanical properties

In Fig. 1a, the engineering and true stress–strain curves of TWIP steel at different strain rates were presented. It can be observed that at the stage of elastic deformation, the stress–strain curves at different strain rates were almost coincident with each other, with the stress increasing rapidly with strain. The initial yield strength (YS), ultimate tensile strength (UTS), buckling strength ratio, and elongation after fracture were found to be 620 MPa, 1039 MPa, 0.6, and 49%, respectively.

Figure 1b plots UTS and YS versus strain rate. It is worth noting that at low strain rates (10^{-4}–10^{-1} s^{-1}), the increase in both UTS and YS of TWIP steel was relatively low, while they increased rapidly at medium strain rates (10^{-1}–10^{2} s^{-1}). It is apparent that UTS decreased from 1168 to 1141 MPa at the strain rate of 10^{3} s^{-1}. It can be seen that the uniform elongation (UE, the plastic elongation percentage at maximum force) and fracture elongation (FE, the engineering strain at failure) increased slowly with increasing strain rate initially, which was followed by a rapid increase. Thus, under quasi-static deformation, TWIP steel has negative strain rate sensitivity [20]. Nevertheless, at intermediate and higher strain rates, it exhibits positive strain rate sensitivity [21].

The strain hardening behavior during tensile testing can be derived from the strain hardening rate ($d\sigma/d\varepsilon$) plots with the true strain (ε). $d\sigma/d\varepsilon$ was obtained by differentiating the true stress–true strain curves shown in Fig. 1c, d. It was found that with the increasing true strain, TWIP steel possesses three distinct strain hardening stages. Only in stage II, $d\sigma/d\varepsilon$ exhibited a plateau between 10^{-4} and 10^{-1} s^{-1}, while in the other stages, it decreased continuously with the increasing strain rate.

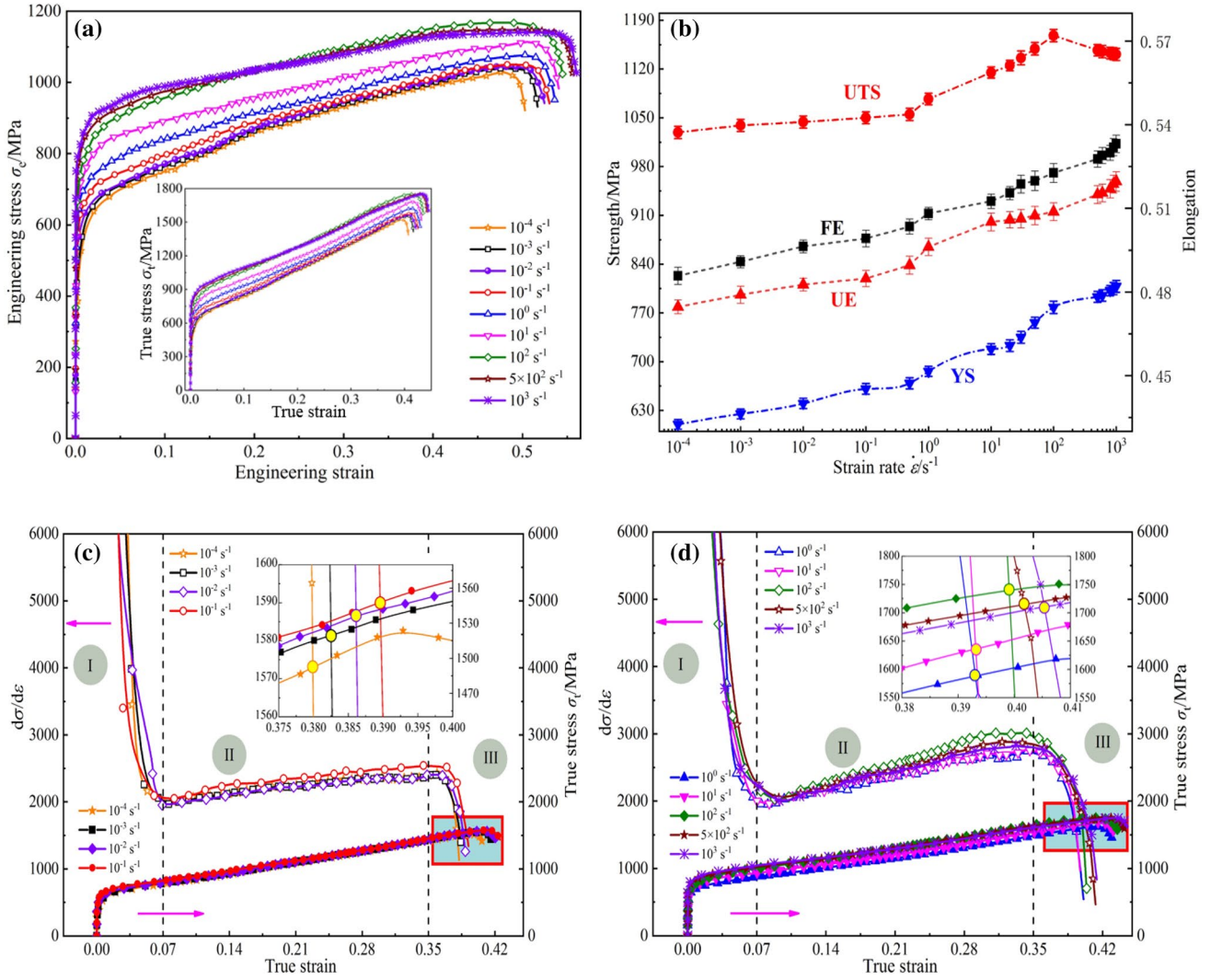

Fig. 1 Mechanical properties of TWIP steel at different strain rates. **a** Engineering and true stress–strain curve; **b** mechanical properties versus strain rate; **c**, **d** strain hardening rate

3.2 Microstructure evolution

In the early stage of tensile deformation of TWIP steel at 10^0 s^{-1}, the dislocation initiated in the austenite grain and then stacked at the grain boundary or the annealing twin boundary (Fig. 2a). Furthermore, stacking faults can be observed, which was due to the fact that the dislocation is easy to expand at the lower dislocation energy [22]. As the deformation increased, the deposition of dislocation plug became more serious, and deformation twins initiated and expanded at the grain boundary, forming a relatively fine lamellar structure (Fig. 2b, c). As the strain increased (until sample fracture), the dislocation density continued to increase and deformation twins parallel to each other expanded to other areas inside the austenite grain, and entangled with a large number of dislocations, resulting in fuzzy grain boundaries (Fig. 2d).

As it can be seen in Fig. 3a, in the early stage of tensile deformation of TWIP steel at a strain rate of 10^2 s^{-1}, many dislocation plugs were deposited at the grain boundaries. Furthermore, more stacking faults were formed at the annealing twin and grain boundaries than those in the sample at 10^0 s^{-1}. When the equivalent true strain increased to 0.2 (Fig. 3b), the deformation twin extended from the grain boundary to the austenite grain with the increase in the deformation twin layer thickness. Figure 3c displays that at a true strain of 0.3, the deformation twins had two crystal orientations in one austenite grain, indicating that two or more twin systems had been actuated. It can be deduced that at higher strain rates, the deformation twins

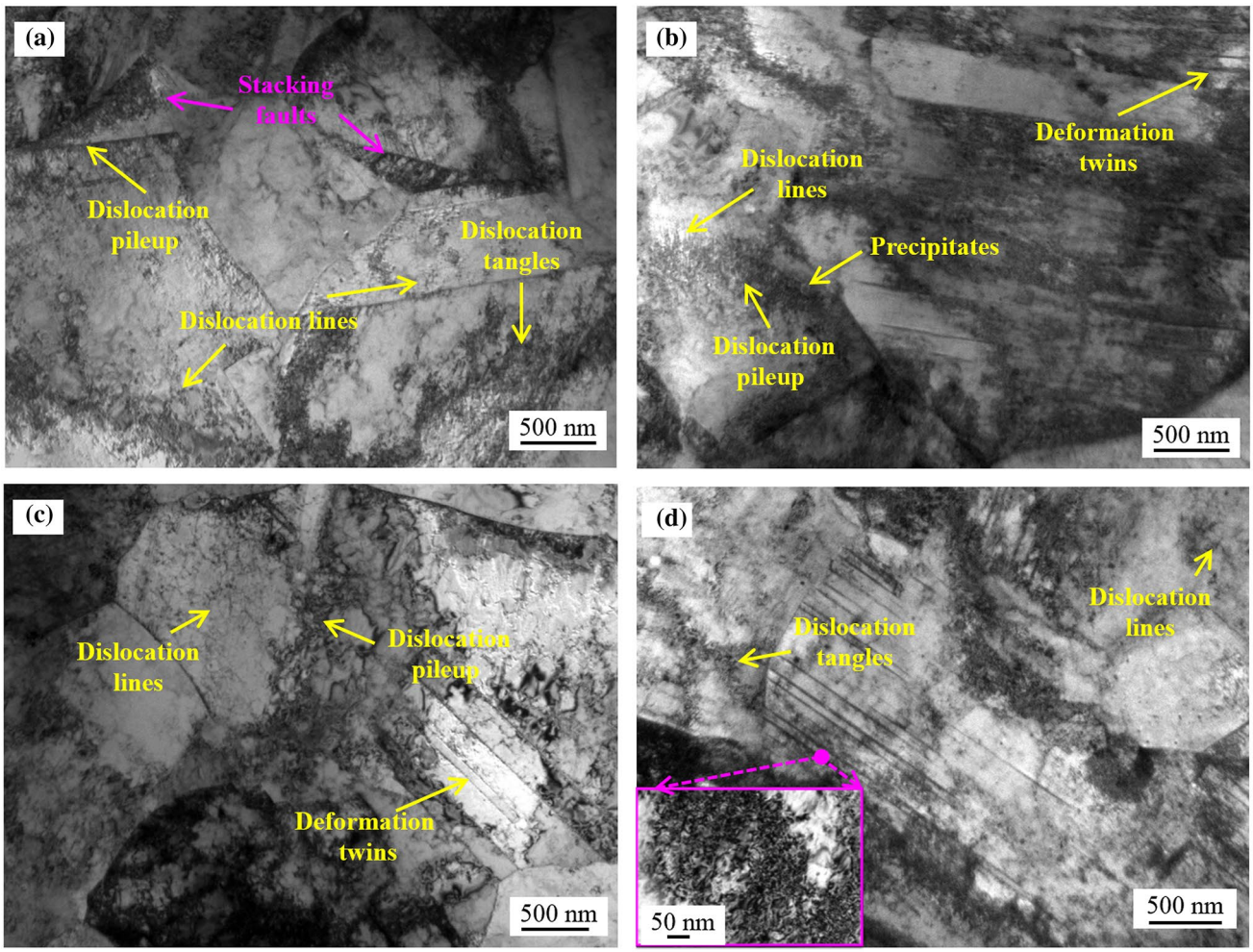

Fig. 2 TEM images of TWIP steel under different deformations at a strain rate of 10^0 s^{-1}. **a** 0.1; **b** 0.2; **c** 0.3; **d** fracture location

are formed following a favorable orientation inside the grain. Deformation twins with different orientations can expand to a region inside the grain and interlace with each other, resulting in the development of multi-beam deformation twins. Consequently, this will further improve the strength and plasticity of the material [23]. After tensile fracture, the deformation twin penetrated almost throughout the entire austenite grain (Fig. 3d) and the initial deformation twin formed a finer secondary deformation twin. The secondary deformation twin will chip the initial twin layers, causing interactions between the secondary deformation twin and the initial deformation twin, which will improve the work hardening rate of the tested steel with uniform elongation. As it can be observed in Fig. 3d, the angles between the two twin systems of the secondary and initial deformation twins were about 68° and 69°, which is in accordance with the angle range of 68°–71° measured by Jeong et al. [24]. In addition, the boundary between the secondary and initial deformation twins contained high-density dislocation structures, which made the boundary of some deformation twins fuzzy.

Figure 4a shows that in the initial deformation of TWIP steel at a strain rate of 10^3 s^{-1}, a large number of dislocation tangles appeared in the austenite grain boundary and around the grain boundary of precipitates. As the deformation increased, there were fine deformation twins and lamination, while in the austenite grain with the relatively narrow twin-chip layer, there was only one oriented deformation twin, most of which terminated in the grain, while small parts ran through the entire grain (Fig. 4c). Moreover, it can be observed that all samples with different deformation levels contained high-density dislocations, which were mixed in the deformation twins, making the twin boundary fuzzy. Contrary to the microstructural changes at 10^2 s^{-1}, no secondary deformation twins were observed in the entire tensile deformation process of TWIP steel at 10^3 s^{-1}. This can be attributed to the high deformation rate, since the strain energy cannot diffuse in a very short period of time,

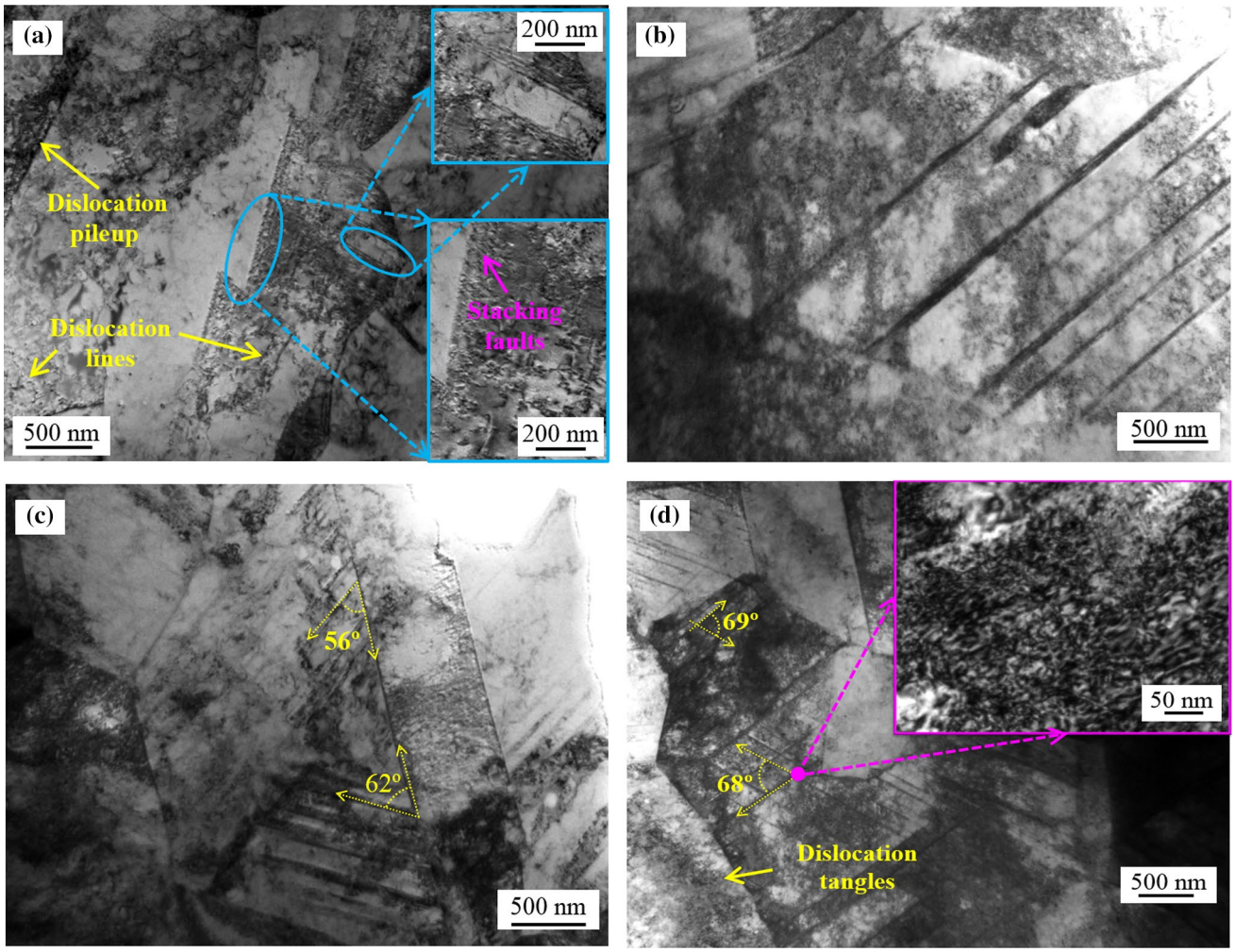

Fig. 3 TEM images of TWIP steel under different deformations at a strain rate of 10^2 s^{-1}. **a** 0.1; **b** 0.2; **c** 0.3; **d** fracture location

resulting in the local increasing temperature of the tested steel. Furthermore, this increases the dislocation mobility and reduces the degree of dislocation pileup at the initial twin boundary, annealing twin boundary, and grain boundary. Thereby, reducing the opportunity of the secondary deformation twin and the initial formation of the deformation twin leads to a decrease in the tensile strength of TWIP steel.

4 Discussion

Figure 5 illustrates the schematic diagram of the microstructure evolution of TWIP steel when plastic deformation occurs at different strain rates. It can be seen that the deformation process is affected by the interaction between deformation twins, grain boundary, and dislocations [25–27]. The density of dislocations increases with the increase in deformation level, and it is mainly distributed at the austenite grain, annealing twin boundary, or deformation twin boundary when the deformation twin initiates and expands. The presence of deformation twins in the tested steel can significantly decrease the size of the austenite grains and shorten the mean free path of dislocation, improving the work hardening rate. In addition, the formation of the secondary deformation twin further increases the dislocation through the twin boundary barrier, and inhibits dislocation annihilation. Consequently, TWIP steel has a high work hardening rate when deformed at a strain rate of 10^2 s^{-1} (Fig. 1d), which guarantees high strength and elongation at the strain rate. When the strain rate is higher (10^3 s^{-1}), the adiabatic temperature rise of the tested steel was more than 140 °C. It led to increase in the mobility of dislocations, inhibiting the occurrence of secondary twinning. Furthermore, the stacking fault energy of ultra-high-yield strength TWIP steel increased to about 30 mJ/m^2, which had a certain inhibition on the formation of deformation twin. In other words, the enhancement effect of the deformation twin boundary

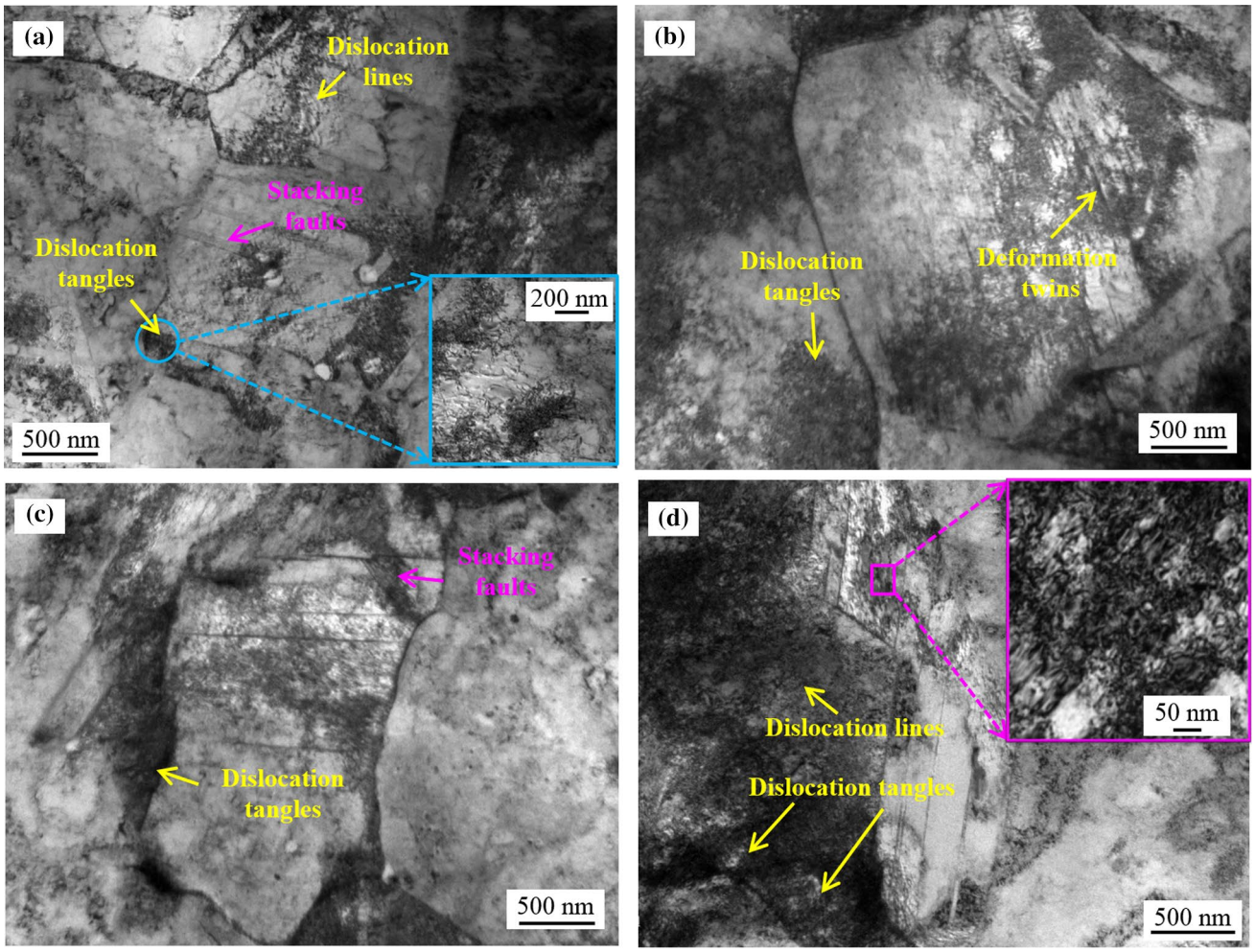

Fig. 4 TEM images of TWIP steel under different deformations at a strain rate of 10^3 s^{-1}. **a** 0.1; **b** 0.2; **c** 0.3; **d** fracture location

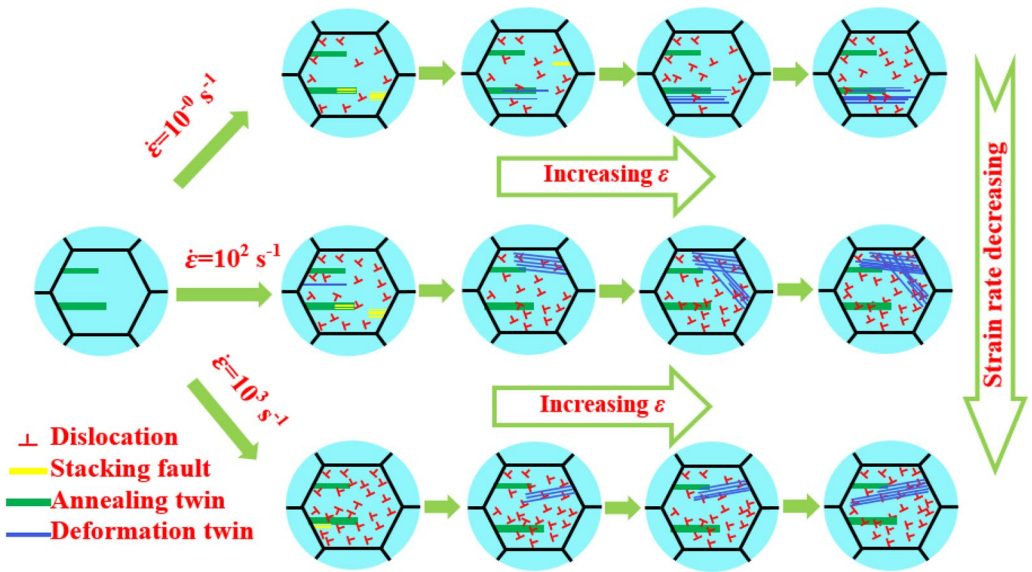

Fig. 5 Schematic diagram of microstructure evolution process of TWIP steel when plastic deformation occurs at different strain rates

satisfies the Hall–Petch relation [28, 29]. It can be seen that due to the formation of deformation twins, the variation trend of work hardening behavior, strength, and plasticity of TWIP steel changes synchronously in the plastic deformation. In this deformation process, the deformation twin mechanism and the dislocation slip mechanism coexist and are highly dependent on the increase in strain rate.

A relevant study [30] has shown that the fraction of nanometer or micro-nanometer sized deformation twin boundaries also increases with the increase in strain during plastic deformation; however, it has not been quantified. Therefore, this paper further investigated the relationship between deformation twins and deformation amount in TWIP steel under dynamic loading with strain rates of 10^0 and 10^2 s^{-1} and equivalent true strains of 0.1, 0.2, 0.3 and 0.4 (fracture location). The sampling position and observation area of EBSD sample are presented in Fig. 6, where t_i ($i=1, 2, 3$) is the thickness of sample i after deformation and ε_i^{eq} is the equivalent true strain of sample i.

Figure 7 shows the relationship between true stress, work hardening rate and twin boundary fraction with true strain in TWIP steel at strain rates of 10^0 and 10^2 s^{-1} under different deformation levels. It is indicated that at both strain rates, the fraction of the deformation twin boundary increases with plastic deformation. More specifically, when the strain rate is 10^0 s^{-1}, the increasing rate of the twin boundary fraction initially increases and then decreases. The DoseResp function of the Origin 9.0 software (Origin Lab, Northampton, MA, USA) was used for fitting. As it can be seen in Fig. 8a, the correlation coefficient R^2 reached 99.32% indicating a high fitting degree. Moreover, when the strain rate was 10^0 s^{-1}, the twin growth law was in line with S curve change resulted from the DoseResp model. At a strain rate of 10^2 s^{-1} (Fig. 8b), the twin boundary fraction increases with the increase in deformation, and R^2 of the linear fitting reached 98.54%, suggesting a good fitting degree. The above observation indicates that the twin boundary fraction under different deformation levels increases almost linearly at a strain rate of 10^2 s^{-1}.

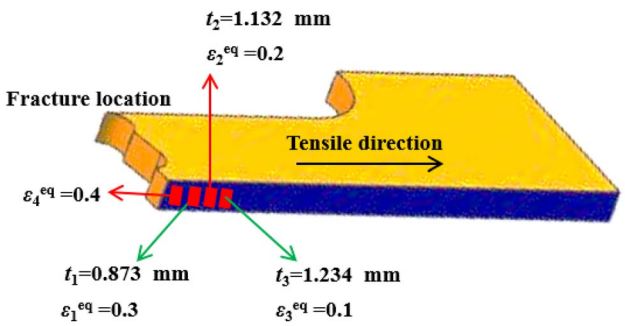

Fig. 6 Schematic diagram of observation area of EBSD sample

Figure 8 displays the variation trend of the twin boundary fraction in TWIP steel with equivalent true strain at strains of 10^0 and 10^2 s^{-1} and the fitting curves. As it can be seen in Fig. 8a, when the deformation occurs at a strain rate of 10^0 s^{-1}, the twin boundary fraction is almost unchanged and small in the equivalent true strain < 0.1. This can be attributed to the fact that the formation of deformation twins requires a certain amount of stress concentration, and deformation twins will be generated when the local stress is large enough to overcome the critical shear stress of nucleation. When the equivalent true strain is within the range of 0.1–0.3, the twin boundary fraction increases almost linearly with the increase in deformation and then increases slowly or remains unchanged. Moreover, when the amount of deformation is small, the twin boundary fraction increases rapidly, which is because at low strain, there are fewer twins in the material, and more grains are produced by the deformation twins. In addition, the interactions between twins and dislocations are weak, which is beneficial for twins with higher work hardening rate (Fig. 7a). When the amount of deformation is large, a moderate number of twins are generated in the early stage of deformation. The interaction between large numbers of dislocations and grain boundary increases the twin shear resistance and hinders the growth of twins. This results in a slow increase or even no increase in the number of twin boundaries, while at the same time, the work hardening rate increases slowly or decreases. Figure 8b demonstrates that the twin boundary fraction increases almost linearly with the increase in deformation level at a strain rate of 10^2 s^{-1}.

The twin boundary fraction at 10^2 s^{-1} is higher than that at 10^0 s^{-1} at each corresponding deformation level (Fig. 8). This is because at a strain rate of 10^2 s^{-1}, the deformation rate is faster, and the density of dislocations is higher. A large number of dislocation microstructures are formed, which provides more potential crystal nuclei for the twins and results in the formation of more deformation twins in the subsequent deformation process. This leads to a significant upward trend in the work hardening rate of the tested steel, which can be observed in Fig. 7b. It can be seen that twins are formed gradually during deformation, and the speed of twin generation is faster at 10^2 s^{-1} than at 10^0 s^{-1}. Moreover, the twin boundary fraction at 10^2 s^{-1} is higher, and the density of dislocations is larger at the corresponding deformation level. Both the twins and the density of dislocations promote and restrict each other, and their synergism affects the mechanical behavior of TWIP steel. Figure 2 indicates that at low strain rates (10^{-4}–10^{-1} s^{-1}), the speed of twin generation is relatively slow, while the dislocation density increases more slowly than at high strain rates. Therefore, the increase in strength and plasticity at low strain rates is slow. To conclude, the changes in the mechanical behavior of TWIP

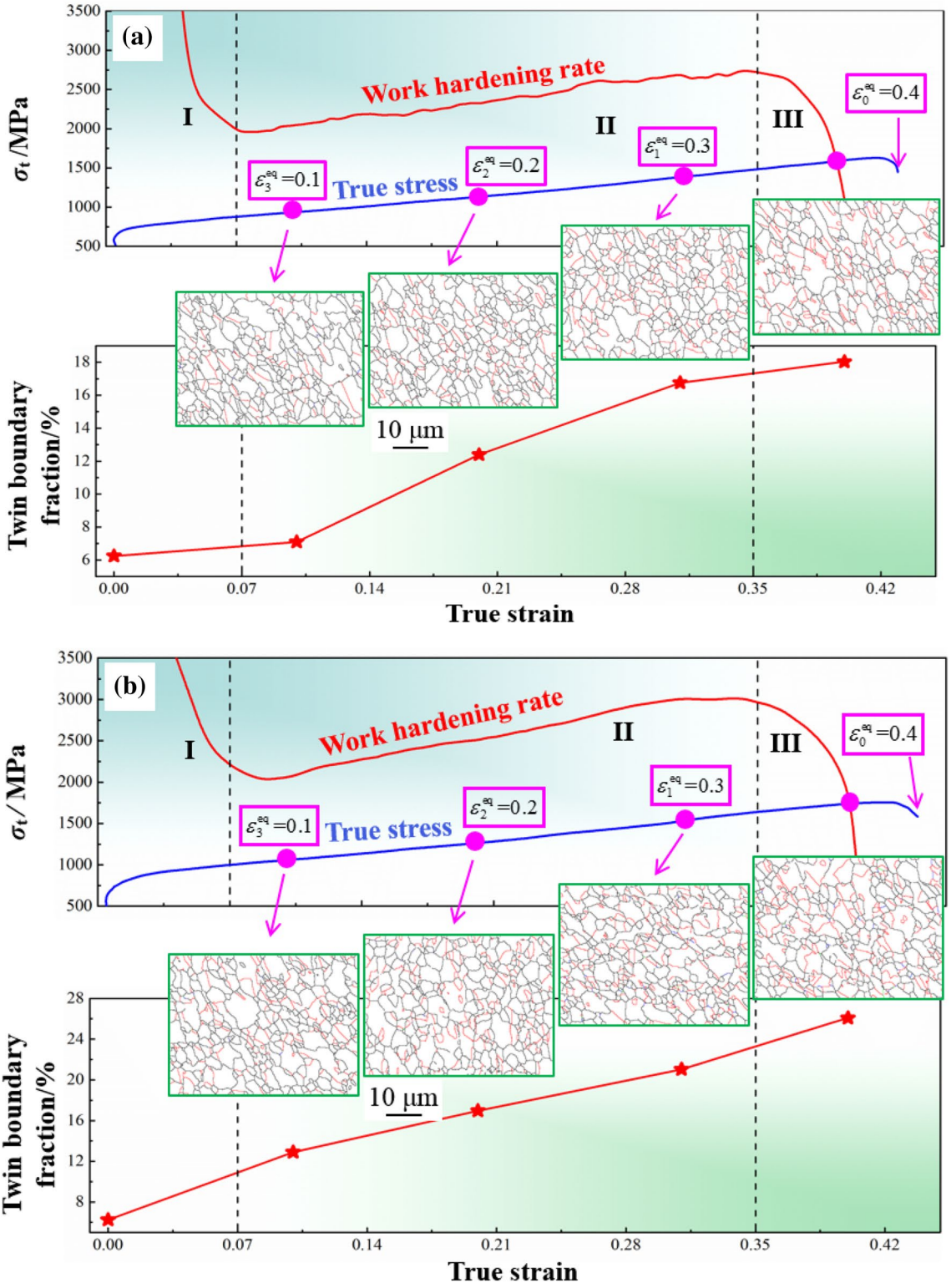

Fig. 7 Changes of work hardening rate, true stress (σ_t), and twin boundary fraction with true strain at a strain rate of 10^0 s^{-1} (**a**) and 10^2 s^{-1} (**b**)

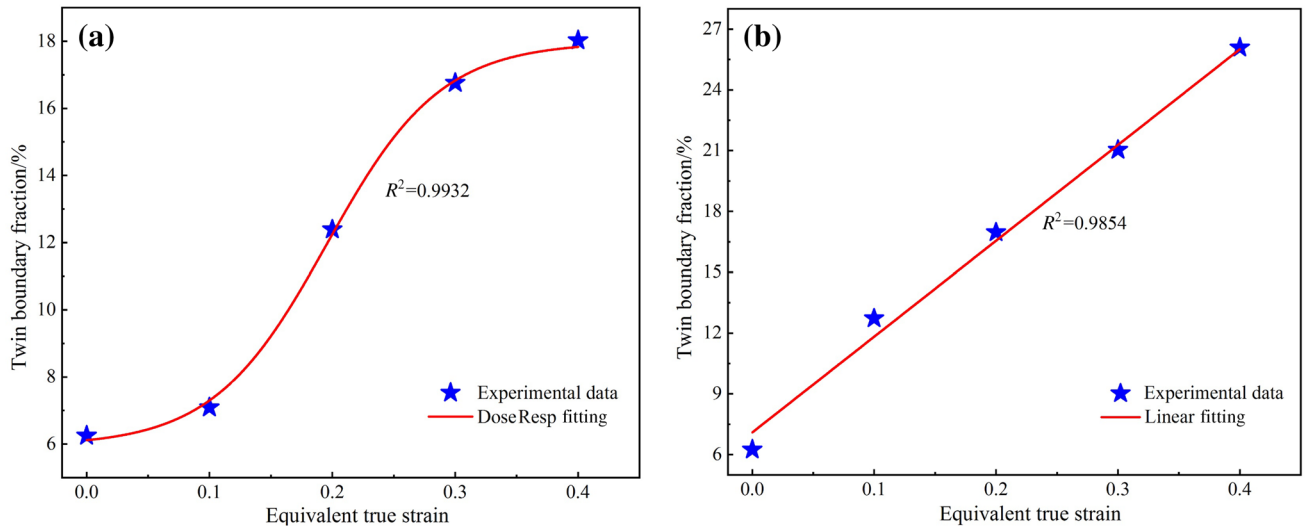

Fig. 8 Change of twin boundary fraction with equivalent true strain and corresponding fitting curves at a strain rate of 10^0 s^{-1} (**a**) and 10^2 s^{-1} (**b**)

steel at different strain rates are the macroscopic reflection of microstructure evolution during plastic deformation.

5 Conclusions

1. The strain rate has a significant effect on the twin morphology of TWIP steels. Under quasi-static deformation, the number of deformation twins is small and the layers of twins are thick. With the increase in strain rate, the twin layer becomes even. Secondary deformation twins were observed at a strain rate of 10^2 s^{-1}, which intersected with the initial deformation twins and increased the resistance of dislocation movement, as well as the strong plasticity.
2. At a strain rate of 10^2 s^{-1}, TWIP steel exhibited a higher twin formation speed than at 10^0 s^{-1}. At corresponding amounts of deformation, the twin boundary fraction was found to be higher and increase linearly at 10^2 s^{-1}, while the rule of twin growth at 10^0 s^{-1} conformed to S-curve change resulted from the DoseResp model.
3. The plastic deformation of the investigated TWIP steel is a mutual promotion and restriction process between deformation twins and dislocation slip. Their synergistic action changes the trends of work hardening rate, strength, and plasticity synchronously. The changes in mechanical behavior at different strain rates are the macroscopic reflection of microstructure evolution during plastic deformation.

Acknowledgements This work is funded by the National Natural Science Foundation of China (No. U1860112), the Guidance Plan of Liaoning Natural Science Foundation (No. 2019-ZD-0025), the Key Project of Liaoning Education Department (No. 2019FWDF03) and the Postdoctoral Research Support Project of Hebei (No. B2019003031).

References

[1] P. Matteis, G. Scavino, F. D'Aiuto, D. Firrao, Steel Res. Int. 83 (2012) 950–956.
[2] Y.Z. Tian, Y. Bai, L.J. Zhao, S. Gao, H.K. Yang, A. Shibata, Z.F. Zhang, N. Tsuji, Mater. Charact. 126 (2017) 74–80.
[3] H.L. Yi, L. Sun, X.C. Xiong, Mater. Sci. Technol. 34 (2018) 1112–1117.
[4] J.K. Kim, Y. Estrin, B.C. De Cooman, Metall. Mater. Trans. A 49 (2018) 5919–5924.
[5] M. Madivala, A. Schwedt, U. Prahl, W. Bleck, Int. J. Plast. 115 (2019) 178–199.
[6] Y.F. Shen, N. Jia, Y.D. Wang, X. Sun, L. Zuo, D. Raabe, Acta Mater. 97 (2015) 305–315.
[7] Y.F. Shen, N. Jia, R.D.K. Misra, L. Zuo, Acta Mater. 103 (2016) 229–242.
[8] J. Chen, J.J. Wang, G. Yuan, C.M. Liu, Mater. Sci. Eng. A 759 (2019) 47–54.
[9] Q.F. Dai, Dynamic deformation constitutive model and micromechanism of 800–1200 MPa ultra-high cold rolled dual phase steel, University of Science and Technology Beijing, Beijing, China, 2013.
[10] H.W. Yen, M. Huang, C.P. Scott, J.R. Yang, Scripta Mater. 66 (2012) 1018–1023.
[11] B.C. De Cooman, Y. Estrin, S.K. Kim, Acta Mater. 142 (2018) 283–362.
[12] Y. Chen, Y.J. Luo, Y.F. Shen, Y. Liu, R.D.K. Misra, Mater. Sci. Eng. A 767 (2019) 138415.
[13] S. Lee, Y. Estrin, B.C. De Cooman, Metall. Mater. Trans. A 45 (2014) 717–730.
[14] Y.F. Shen, Y.D. Wang, X.P. Liu, X. Sun, R.L. Peng, S.Y. Zhang, L. Zuo, P.K. Liaw, Acta Mater. 61 (2013) 6093–6106.
[15] J.K. Kim, L. Chen, H.S. Kim, S.K. Kim, Y. Estrin. B.C. De Cooman, Metall. Mater. Trans. A 40 (2009) 3147–3158.

[16] O. Bouaziz, S. Allain, C.P. Scott, P. Cugy, D. Barbier, Current Opinion Solid State Mater. Sci. 15 (2011) 141–168.
[17] O. Grässel, L. Krüger, G. Frommeyer, L.W. Meyer, Int. J. Plast. 16 (2000) 1391–1409.
[18] G. Frommeyer, U. Brüx, P. Neumann, ISIJ Int. 43 (2003) 438–446.
[19] S.Q. Xu, D. Ruan, J.H. Beynon, Y.H. Rong, Mater. Sci. Eng. A 573 (2013) 132–140.
[20] X.K. Ma, F.G. Li, J. Cao, J.H. Li, Z.K. Sun, G. Zhu, S.S. Zhou, Mater. Sci. Eng. A 710 (2018) 1–9.
[21] G.T. Gray III, Ann. Rev. Mater. Res. 42 (2012) 285–303.
[22] X.H. An, S. Qu, S.D. Wu, Z.F. Zhang, J. Mater. Res. 26 (2011) 407–415.
[23] Y.G. Yang. Z.L. Mi, H. Li, M. Xu, R.T. Jiang, Steel Res. Int. 89 (2018) 1–8.
[24] K. Jeong, J.E. Jin, Y.S. Jung, S. Kang, Y.K. Lee, Acta Mater. 61 (2013) 3399–3410.
[25] D.T. Pierce, J.A. Jiménez, J. Bentley, D. Raabed, J.E. Wittige, Acta Mater. 100 (2015) 178–190.
[26] K. Renard, H. Idrissi, D. Schryvers, P.J. Jacques, Scripta Mater. 66 (2012) 966–971.
[27] I. Gutierrez-Urrutia, D. Raabe, Scripta Mater. 66 (2012) 992–996.
[28] L. Bracke, K. Verbeken, L. Kestens, J. Penning, Acta Mater. 57 (2009) 1512–1524.
[29] L. Lu, Y.F. Shen, X.H. Chen, L.H. Qian, K. Lu, Science 304 (2004) 422–426.
[30] P. Chowdhury, D. Canadinc, H. Sehitoglu. Mater. Sci. Eng. R Rep. 122 (2007) 1–28.